Dynamic single-molecule sensing by actively tuning binding kinetics for ultrasensitive biomarker detection

Qiang Zeng[a,1], Xiaoyan Zhou[a,1], Yuting Yang[b,1], Yi Sun[c], Jingan Wang[a], Chunhui Zhai[a], Jinghong Li[c,2], and Hui Yu[a,d,2]

[a]School of Biomedical Engineering, Shanghai Jiao Tong University, Shanghai 200030, People's Republic of China; [b]Department of Instrument Science and Engineering, School of Electronic Information and Electrical Engineering, Shanghai Jiao Tong University, Shanghai 200030, People's Republic of China; [c]Department of Chemistry, Key Laboratory of Bioorganic Phosphorus Chemistry and Chemical Biology, Tsinghua University, Beijing 100084, People's Republic of China; and [d]Institute of Medical Robotics, Shanghai Jiao Tong University, Shanghai 200030, People's Republic of China

Edited by Catherine Murphy, University of Illinois at Urbana–Champaign, Urbana, IL; received November 8, 2021; accepted January 29, 2022

The ability to measure many single molecules simultaneously in large and complex samples is critical to the translation of single-molecule sensors for practical applications in biomarker detection. The challenges lie in the limits imposed by mass transportation and thermodynamics, resulting in long assay time and/or insufficient sensitivity. Here, we report an approach called Sensing Single Molecule under MicroManipulation (SSM^3) to circumvent the above limits. In SSM^3, single-molecule binding processes were dynamically recorded by surface plasmon resonance microscopy in a nanoparticle-mediated sandwich scheme. The binding kinetics between analyte and probes are fine-tuned by nanoparticle micromanipulations to promote the repetitive binding and dissociation. Quantifying the heterogeneous lifetime of each molecular complex allows the discrimination of specific binding from nonspecific background noise. By digitally counting the number of repetitive specific binding events, we demonstrate the direct detection of microRNAs and amyloid-β proteins with the limit of detection at the subfemtomolar level in buffer and spiked human serum. Together with the nanoparticle micromanipulation to promote the transportation rate of analyte molecules, the assay could be performed within as short as 15 min without the need for preincubation. The advantages over other single-molecule sensors include short assay time, compatible with common probes and ultrasensitive detection. With further improvement on the throughput and automation, we anticipate the proposed approach could find wide applications in fundamental biological research and clinical testing of disease-related biomarkers.

single molecule | biosensors | ultrasensitive | microRNA | immunoassay

The analytical methods have converged from ensemble measurements of numerous entities to quantized measurements at the single-molecule level. Single-molecule measurements could reveal heterogeneities and stochastic processes within biological systems (1, 2) and set the ultimate detection limit of chemical and biological sensors. By reducing the measurement volume to a few femtoliters, the detection of a single molecule has been realized in various forms [i.e., single-molecule fluorescence (3, 4), nanopores (5, 6), localized surface plasmon resonance (7, 8), and surface-enhanced Raman scattering (9, 10)]. These measurements typically require quantifying many single-molecule events to gain new molecular and mechanistic insights or to achieve better analytical performance. However, it has been difficult to perform quantitative analysis with sufficient efficiency and statistical accuracy because of the concentration limit from mass transportation (11, 12) and the thermodynamic limit from probe affinity (13). For quantification of biomarkers in biological media, in which the required concentrations are usually at the femtomolar level or even lower (14), the single-molecule measurements could take inordinately long, and the nonspecific binding of unwanted species degrades the accuracy.

In the past two decades, several single-molecule approaches for biomarker detection have been developed to surpass the above limits by biasing the equilibrium and driving binding reactions (15, 16). A typical scheme involves the usage of nanoparticles to collect the analyte followed by a digital measurement of single molecules at a confined space (17), such as the commercialized, single-molecule enzyme-linked immunosorbent analysis (digital ELISA) (18). The digital ELISA uses the antibody-modified magnetic beads to capture the analyte in solution and loads them into femtoliter-sized reaction chambers termed single-molecule arrays. It effectively improves the sensitivity of conventional ELISA by three orders with a limit of detection (LoD) at the subfemtomolar level but requires sophisticated devices and excessive operation to remove free analyte molecules. Besides, the performance is still limited by the probe affinity and false positive arising from detection antibodies that bind nonspecifically to assay surface.

A distinct yet effective strategy is to explore the in-depth heterogeneous information of single-molecule interaction (19). Walter et al. first demonstrated a kinetic fingerprinting approach to perform highly specific and sensitive detection of biomarkers via single-molecule fluorescence microscopy (20–22). This single-molecule recognition through equilibrium

Significance

The detection of low-abundance molecular biomarkers is key to the liquid–biopsy-based disease diagnosis. Existing methods are limited by the affinity and specificity of recognition probes and the mass transportation of analyte molecules onto the sensor surfaces, resulting in insufficient sensitivity and long assay time. This work establishes a rapid and ultrasensitive approach by actively tuning binding kinetics and accelerating the mass transportation via nanoparticle micromanipulations. This is significant because it permits extremely sensitive measurements within clinically acceptable assay time. It is incubation-free, washing-free, and compatible with low- and high-affinity probes.

Author contributions: J.L. and H.Y. designed research; Q.Z., X.Z., and Y.Y. performed research; Y.S., J.W., and C.Z. contributed new reagents/analytic tools; Q.Z., Y.Y., and H.Y. analyzed data; and Q.Z., X.Z., Y.Y., and H.Y. wrote the paper.

The authors declare no competing interest.

This article is a PNAS Direct Submission.

[1]Q.Z., X.Z., and Y.Y. contributed equally to this work.

[2]To whom correspondence may be addressed. Email: hui.yu@sjtu.edu.cn or jhli@mail.tsinghua.edu.cn.

This article contains supporting information online at http://www.pnas.org/lookup/suppl/doi:10.1073/pnas.2120379119/-/DCSupplemental.

Published March 1, 2022.

Poisson sampling technique surpasses the thermodynamic limit by exploiting the repetitive binding of fluorescently labeled, low-affinity probes to the analyte (23) and discriminating specific binding from background noise by a kinetic signature. The detection limits of microRNAs (miRNAs) and proteins also reach the subfemtomolar level, but screening probes with unique kinetic property is not compatible with current pipelines, and the concentration limit implies long incubation time before detection.

Herein, we present the integration of single-molecule manipulation and dynamic sensing to allow rapid and ultrasensitive detection of biomarkers beyond the concentration and thermodynamic limits. In this Sensing Single Molecule under Micro-Manipulation (SSM^3) approach, an external force is applied on the molecular bound between analyte and probes through tethered nanoparticles to actively tune the binding kinetics. This strategy, together with a dynamic sensing approach to exploit the heterogeneity at the single-molecule level, is able to beat the limits in both assay time and sensitivity. We show the principle and realization of the SSM^3 technique and demonstrate 15-min assays to directly measure miRNAs and proteins at the subfemtomolar concentration.

Results and Discussion

The Principle. The single-molecule detection was performed in a typical sandwich scheme composed of a high-affinity primary probe immobilized on a planar sensor chip, the analyte, and a secondary probe tethered to nanoparticles (Fig. 1*A*). A microscope with single-nanoparticle imaging capability, such as the surface plasmon resonance microscope (SPRM) used herein, dynamically records the image sequences of nanoparticles to report single molecular interactions (24–27). Considering the first-order binding kinetics between the analyte and the secondary probe, SSM^3 reports the sum of total binding and dissociation events during the observation by digital counting at the single-molecule level (Eq. **1**),

$$N(\tau) = \int_0^\tau (k_{on}[A]_t[P]_t + k_{off}[AP]_t)dt, \quad [1]$$

where k_{on} and k_{off} are the association and dissociation rate constants, [A], [P], and [AP] are the concentration of free analyte, free probes, and the analyte–probe complexes. This readout increases continuously with longer observation time, even after reaching equilibrium, so that the detection limit is only determined by the background noise from nonspecific binding. This is obviously different from the conventional endpoint ensemble measurement in which the limited binding affinity sets the maximum readout (*SI Appendix*).

The SSM^3 also reports the duration of each binding event, which is determined by the binding and dissociation kinetics (28). As a result, we could count only the specific binding in Eq. **1** and obtain an ultrahigh sensitivity beyond the thermodynamic limit. But it is critical to use an appropriate, low-affinity probe with rapid binding and dissociation kinetics so that enough number of dissociation events could be identified for statistical analysis in the limited assay time. SSM^3 makes use of the single-molecule manipulation (29, 30) to fine-tune the

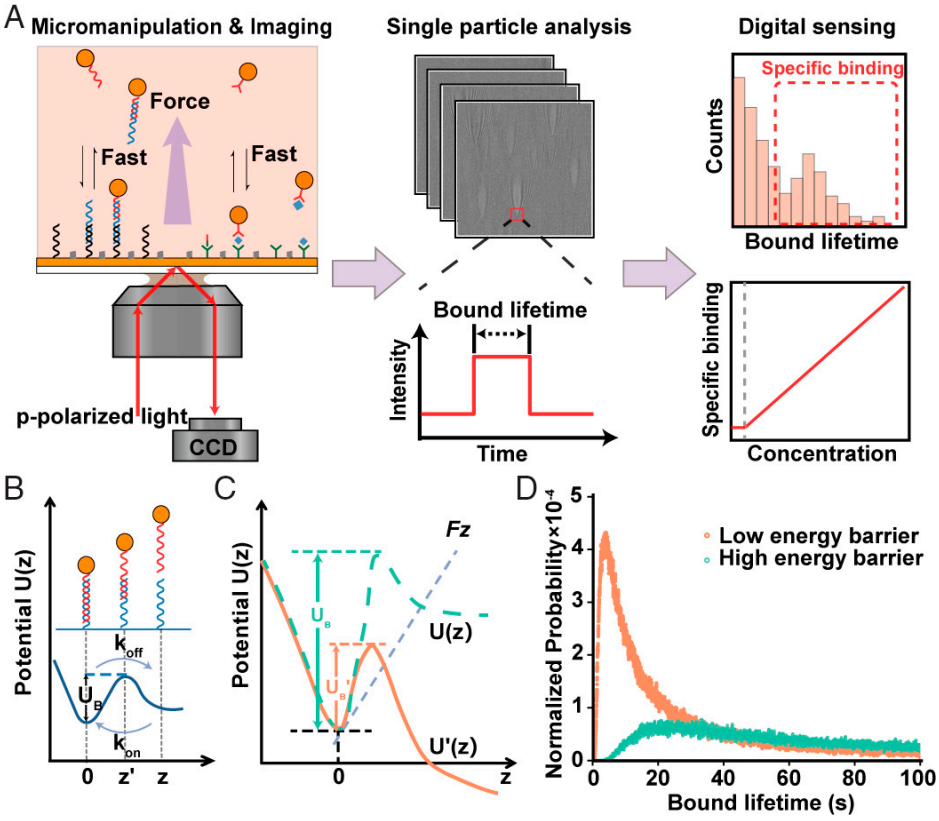

Fig. 1. The principle of SSM^3. (*A*) The SSM^3 actively tunes molecular binding kinetics by single-molecule micromanipulation through nanoparticles; single-nanoparticle imaging with surface plasmon resonance microscopy records the dynamic binding process by a charge-coupled device (CCD) or complementary-metal-oxide-semiconductor (CMOS) image sensor. Data analysis at the single-particle level reveals the dynamic features of specific and nonspecific binding events, and digital counting of only specific events enables ultrasensitive detection of analyte concentration. (*B*) In the one-dimensional elastic model system of single-molecule interaction, the energy barrier U_B determines the binding and dissociation kinetics. (*C*) When applying an external driving potential (purple), the energy barrier height could decrease (orange) from original status (green). (*D*) The molecular bound lifetime is shortened with the decrease of energy barriers, as determined by the Monte Carlo simulation. Detailed parameter setting is described in the *Materials and Methods*.

binding kinetics of commonly used high-affinity probes. Considering the one-dimensional system (Fig. 1*B*), the thermodynamics could be described by the Langevin equation (31),

$$M\frac{d^2z}{dt^2} = -\frac{dU(z)}{dz} - 6\pi\eta a\frac{dz}{dt} + \xi(t), \quad [2]$$

where M is the mass of the nanoparticle, $U(z)$ is the restoring potential related to the molecular binding energy, the second term on the right describes the damping due to viscosity (η is the solvent viscosity and a is the radius of the nanoparticle), and ξ is the thermal fluctuation force. The probability, ρ(t), that a molecule persists in its bound state can be approximately calculated through the kinetic equation as defined by Kramer's transition rate (32),

$$\frac{d\rho(t)}{dt} = -\frac{\omega_0\omega_1 M}{12\pi^2\eta a}e^{-\left(U_B'(t)/K_BT\right)}\rho(t), \quad [3]$$

where U_B' is the barrier height, ω_0 and ω_1 are the effective oscillation frequencies at the bound state and at the maximum potential, K_B is Boltzmann constant, and T is the temperature. The Monte Carlo simulation (*SI Appendix*) shows that when lowering the energy barrier with an external force (Fig. 1*C*), the distribution shifts toward the shorter timescale as expected, and consequently, the frequency of repetitive binding increases (Fig. 1*D*).

The Effectiveness of Micromanipulation. To prove the effectiveness of the nanoparticle micromanipulation and dynamic sensing strategy, we first explored the electrical manipulation of 50-nm Au nanoparticles (AuNPs), owing to the compatibility of SPRM with electrochemical systems (Fig. 2*A*) (33, 34). A 50-nucleotide (nt) oligoanalyte and two 25-nt DNA probes were synthesized (Table S1) as a model system. With the concentration of AuNPs at 10^{10}/mL (~16 pM), the chance of more than one analyte molecule binding to one AuNP is less than 1.8% at an analyte concentration below 3.2 pM, according to the Poisson statistics (35). When examining the distribution of bound lifetime, the specific binding to the oligoanalyte could be discriminated from nonspecific binding (Fig. 2*B*). This was confirmed by the nonspecific binding in the control group with the absence of analyte, in which most nanoparticles hit and ran quickly, and a very small portion was adsorbed on surface firmly. (*SI Appendix*, Fig. S1).

The mean lifetime for nonspecific binding in the control experiments was found to be 4.11 ± 0.26 s (mean ± SD, n = 3) by fitting the full-spectrum data from 0 to 100 s with an exponential function (*SI Appendix*, Fig. S2). A threshold value at 5 s (mean + 3 × SD of the mean lifetime of nonspecific binding) was set to exclude nonspecific events and to keep a large number of specific events. The lifetime of specific binding over the threshold was fitted to find the mean lifetime, which reflects the potential barrier height as in Eq. **3**. When the voltage was at 0 V, the mean lifetime of molecular complexes was found to be 35.04 ± 1.21 s (Fig. 2*C*), which corresponds well to the expectation for probes with a typical dissociation constant in the micromole-to-nanomole range (28). With a negative voltage applied, the AuNPs (zeta potential: −31.67 mV; Table S2) were driven away from the surface. The mean lifetime thus decreased, and the readout in Eq. **1** increased. Note that when the energy barrier diminished at a higher negative voltage, it largely impeded the binding process and the readout did not

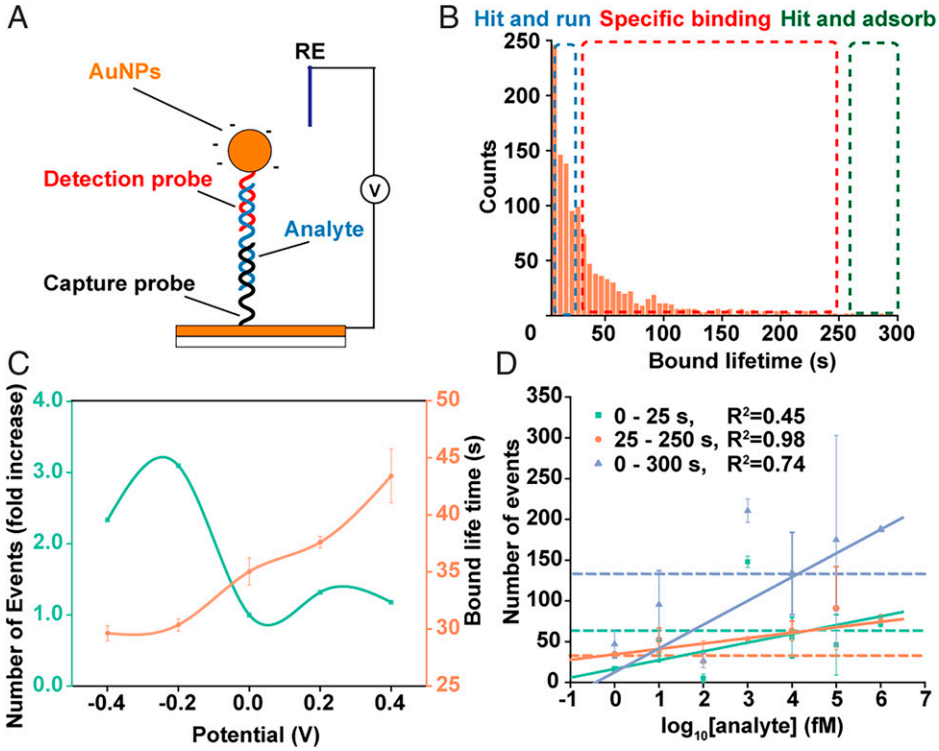

Fig. 2. Effect of nanoparticle manipulation on the single-molecule sensing performance. (*A*) The SSM^3 system for miRNA detection consists of the Au film-'capture probe'–analyte-'detection probe'–AuNP sandwich structure and a potentiostat for electrical manipulation of the 50 nm AuNP. (*B*) The lifetime distribution of binding events in the 50-nt oligoanalyte detection, the corresponding windows of the nonspecific hit-and-run (blue dashed box) and hit-and-adsorb (green) behavior, and the specific binding (red). (*C*) The mean lifetime and the number of events recorded with different applied voltages (fold increase over the number of events at 0 V). (*D*) The calibration curves for determining the 50-nt oligoanalyte concentration by the number of events within different lifetime windows. The dashed lines indicate the baseline levels in control experiments with the absence of analyte (mean + 3 × SD of the number of events).

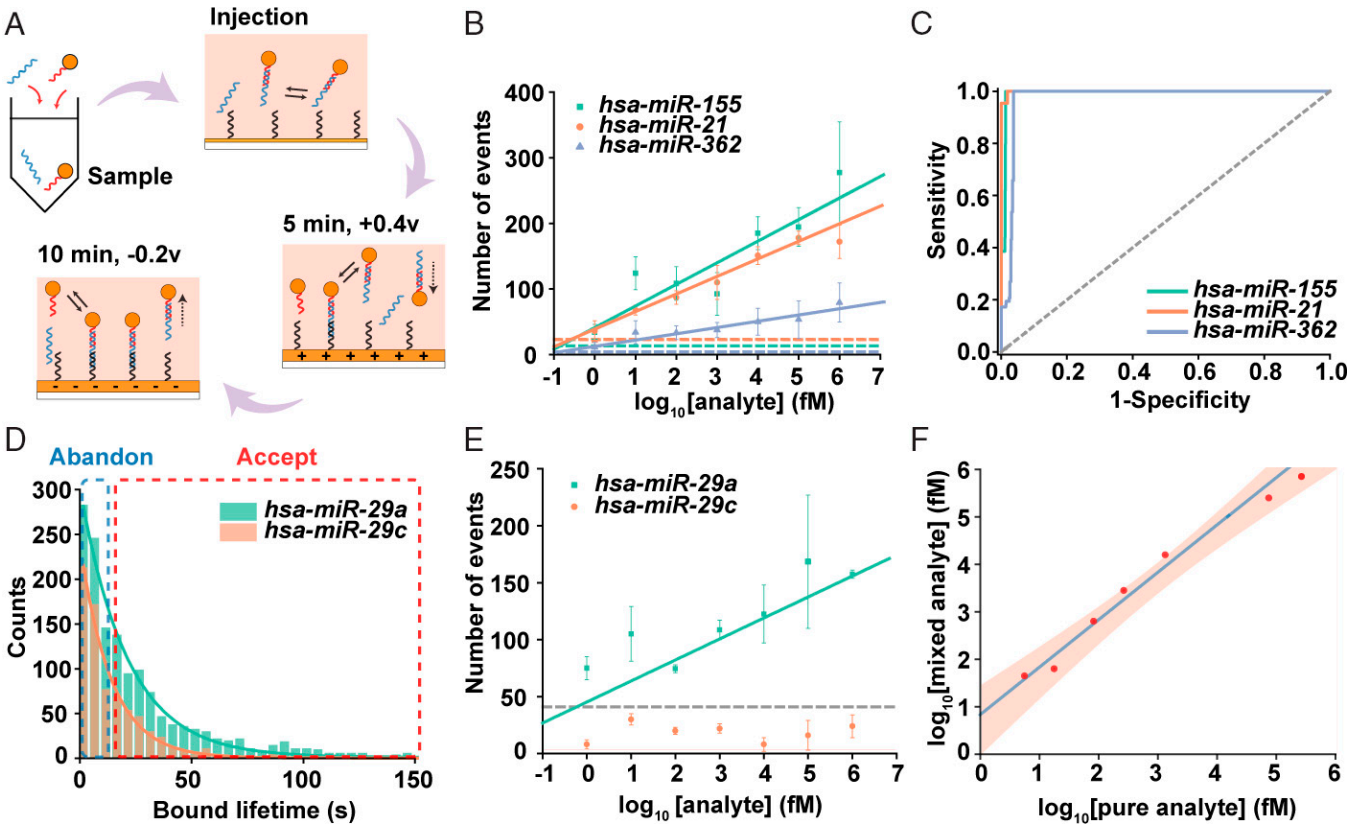

Fig. 3. The rapid miRNA-testing assay. (*A*) The workflow of 15-min miRNA assay includes mixing samples with probe-tethered nanoparticles, injecting the mixture into the reaction chamber, and continuously recording for 5 min at +0.4 V and 10 min at −0.2 V. The calibration curves (*B*) and the receiver-operating characteristics (*C*) for *hsa-miR-21–5p, hsa-miR-155–5p*, and *hsa-miR-362–5p* detection. (*D*) The lifetime distribution of molecular bound between the probes (complementary to *hsa-miR-29a*) and *hsa-miR-29a* or *hsa-miR-29c*. (*E*) The calibration curves of *hsa-miR-29a* and *hsa-miR-29c* detection. (*F*) Measured concentrations of the *hsa-miR-29a* with (vertical axis) versus without (horizontal axis) the interference of *hsa-miR-29c* at a 100-fold higher concentration. The shadow region indicates the 95% confidence region as determined by Student's *t*-test. The dashed lines in calibration curves indicate the baseline level determined with the absence of analyte.

further increase. Empirically, the optimal manipulation was found at −0.2 V, in which the mean lifetime decreased to 29.64 ± 0.65 s, and the readout increased by up to threefold.

The discrimination of specific binding by the lifetime of molecular complex leads to improved LoD. The LoD was defined as the analyte concentration to generate the number of events that equals (mean + 3 × SD) of the number of events in the control experiments. The LoD by direct counting of all events within the 0 to 300 s lifetime window was 14.88 pM, which is similar to the previously reported digital assay (24, 36). When counting only specific binding within the 25- to 250-s window, within which over 95% of the nonspecific binding was discarded, the LoD was found to be 0.36 fM with a high linearity (Fig. 2*D*). Although a large number of events were rejected, most of them were due to the nonspecific bindings, as could be seen from the significant lowering of baseline (dashed lines). When examining the results within 0 to 25 s, it shows a poor linearity as the nonspecific binding dominates. These results thus proved the effectiveness of using in-depth heterogeneous information at the single-molecule level to improve the sensing performances.

Rapid miRNA-Testing Assay. We then demonstrated the capability of SSM[3] in developing the 15-min assay to detect miRNAs (Fig. 3*A*). DNA probes with 12 nt complementary to the target miRNA were tethered to the AuNPs, while high-affinity locked nucleic acid probes were immobilized on the planar Au sensor surface as the capture probes. At a low concentration, the preincubation of analyte on the coated planar sensor could take tens of minutes, resulting in long assay time. Instead, in SSM[3], the analyte was mixed with the probe-coated AuNPs and immediately injected into the testing chamber without further incubation. A voltage was applied sequentially as +0.4 V for 5 min to facilitate transportation of analyte and AuNPs onto the sensor surface, followed by −0.2 V for 10 min to promote repetitive binding. The image sequences were recorded immediately after injection and continuously throughout the assay. Within 15 min, the time-dependent coefficient of variation decreased to below 15%, indicating that the assay time is enough to reach a good stability in readout (*SI Appendix*, Fig. S3).

To prove the effectiveness and generality, we tested three synthetic, disease-related miRNAs, including *hsa-miR-21–5p* (*miR-21*), *hsa-miR-155–5p* (*miR-155*), and *hsa-miR-362–5p* (*miR-362*), with corresponding probes (Table S3). The mean lifetime was found to be 16.54 ± 1.76 s for *miR-21*, 17.14 ± 1.48 s for *miR-155*, and 16.35 ± 1.75 s for *miR-362* (*SI Appendix*, Fig. S2 *A–C*). Although the lifetime was shorter than that of the above 50-nt oligoanalyte system because of the lower affinity, specific binding events could be well distinguished from nonspecific events by setting the threshold as 5 s. The LoD for *miR-21*, *miR-155*, and *miR-362* were found to be 0.26, 0.17, and 0.15 fM, respectively, with linear detection ranges over six orders of magnitude (Fig. 3*B*). In the receiver operating characteristic plot, the area under curve (AUC) values were 0.997, 0.988, and 0.967, respectively (Fig. 3*C*). In principle, a more

rigorous threshold setting could further improve the specificity but at the cost of less countable events and consequently longer assay time.

The 15-min SSM^3 assay could also be used to discriminate single-base mismatch, owing to its high specificity. Two disease-related miRNAs, the *hsa-miR-29a* and *hsa-miR-29c*, were synthesized with a single-nt difference, and the detection probe was 12 nt complimentary to *hsa-miR-29a* (Table S4). The mean lifetime of *hsa-miR-29a* and *hsa-miR-29c* binding to the probes were found to be 21.47 ± 0.45 s and 10.42 ± 0.96 s, respectively (Fig. 3*D*). We, thus, empirically set a threshold at 14 s to discard the majority of events from *hsa-miR-29c* and found that the tests only show dependency on the concentration of *hsa-miR-29a* (Fig. 3*E*). The distinct sensing performance guarantees high specificity with a discrimination factor over 141 for detection of *hsa-miR-29a* and *hsa-miR-29c*. In the presence of *hsa-miR-29c*, at a 100-fold higher concentration, the LoD of *hsa-miR-29a* was found to be 0.63 fM with an AUC of 0.816 (*SI Appendix*, Fig. S4). The detection of *hsa-miR-29a* with or without the existence of *hsa-miR-29c* corresponds well with each other, thus further verifying the effectiveness (slope = 0.92, $R > 0.99$) (Fig. 3*F*).

SSM^3 Immunoassay. The SSM^3 is also compatible with the immunoassay for protein detection by replacing the DNA probes with corresponding antibodies. We then demonstrate the ultrasensitive detection of beta amyloid protein 42 ($A\beta_{1-42}$), an important molecular biomarker for neurodegenerative disease diagnostics in body fluid. Primary antibodies were coated on the planar sensor surface and on AuNPs in the sandwich system (Fig. 4*A*). Under the optimized condition, the electrical manipulation shortened the mean lifetime for protein detection from 45.05 ± 1.36 s to 29.63 ± 1.03 s (Fig. 4*B*), and the LoD for $A\beta_{1-42}$ detection reached 4.34 fg/mL (1.08 fM) (Fig. 4*C*) by setting the 5-s threshold. Note that the mean lifetime of ∼45 s in immunoassay is longer than that of ∼17 s in miRNA assay because of the higher affinity between protein and antibody interaction, imposing the requirement for a higher applied force.

To further improve the performance, we introduced the magnetic-manipulation scheme, which has been used in magnetic tweezers to provide the pico–Newton level force to break down molecular complexes (37). The magnetic manipulation involves the use of 300-nm magnetic nanoparticles (MNPs) and external magnetic fields to replace the AuNPs and electric fields (Fig. 4*A*). The binding kinetics between $A\beta_{1-42}$ proteins and antibodies could be adjusted in a wider range by changing the distance between the magnet and the sensor surface, reducing the bound lifetime to 17.59 ± 1.80 s (Fig. 4*B*). Under optimal experimental conditions, the LoD via magnetic manipulation was found to be 0.21 fg/mL (0.05 fM), which is 20 times better than that via electrical manipulation (Fig. 4*C*).

Spiked miRNA and Protein Test in Human Serum. To further verify the effectiveness of SSM (3) assay in complex samples, we performed the 15-min assay to detect *hsa-miR-29a* and $A\beta_{1-42}$ proteins spiked in human serum. Under electrical manipulation, the LoD for spiked *hsa-miR-29a* detection was 1.51 fM (Fig. 5*A*). As the $A\beta_{1-42}$ protein level in human serum is usually on the level of picograms per milliliter (38), we pretreated the serum by proteinase K to digest existing proteins, followed by a 90 °C treatment to further inactivate remaining proteins. The LoDs for spiked $A\beta_{1-42}$ protein detection in the pretreated human serum were 21.87 fg/mL (4.84 fM) via electrical manipulation and 6.76 fg/mL (1.49 fM) via magnetic manipulation (Fig. 5*B*). With this calibration curve, we then directly measured the $A\beta_{1-42}$ protein level in untreated human serum samples, yielding the concentration of 18.93 ± 3.73 pg/mL (mean ± SD, $n = 3$) that is within the typical range reported (38, 39).

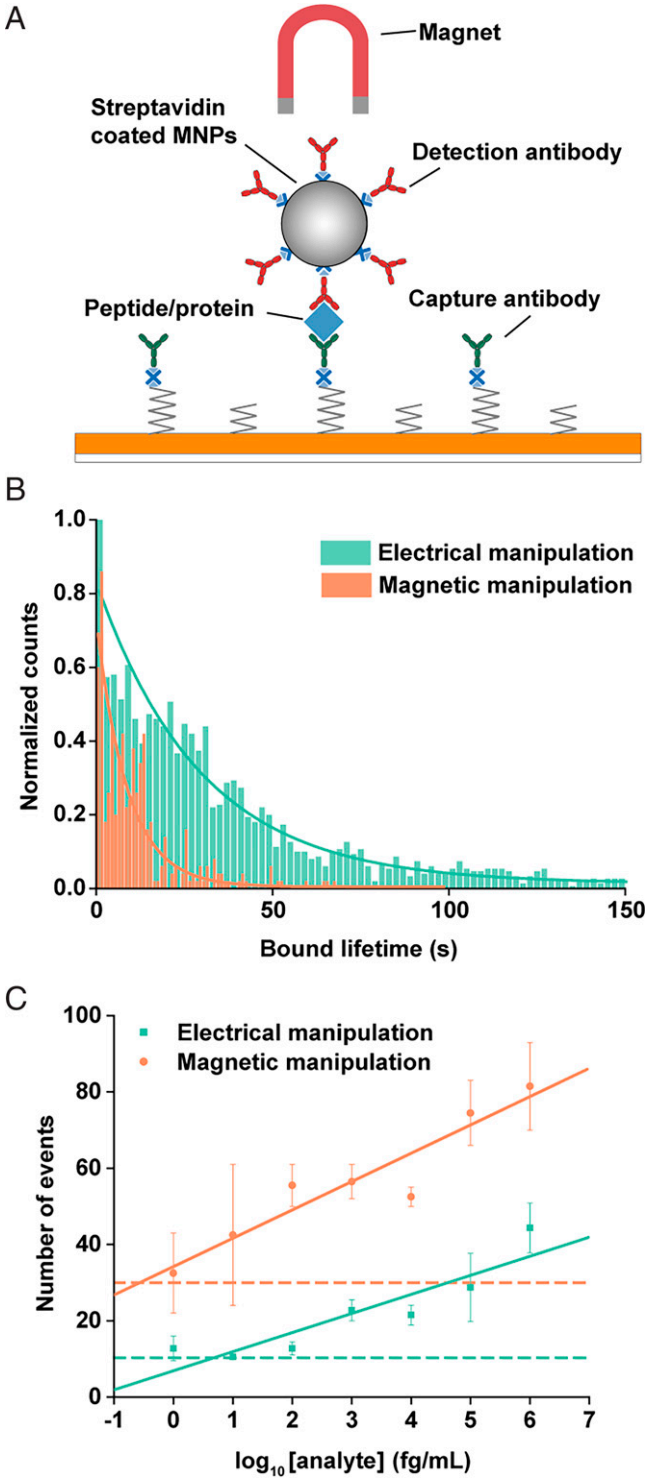

Fig. 4. The rapid immunoassay for $A\beta_{1-42}$ protein detection. (*A*) The SSM^3 system with magnetic manipulation for immunoassay consists of the Au film-antibody–'protein analyte'-antibody–MNP sandwich structure and a magnet for manipulation of the 300-nm MNP. (*B*) The bound lifetime of $A\beta_{1-42}$ protein–binding events under optimal magnetic manipulation (orange) is shorter than that under electrical manipulation at −0.4 V (green). (*C*) The calibration curves of protein concentration under electrical and magnetic manipulations. The dashed lines indicate the baseline level with the absence of analyte.

We have presented the SSM^3 for ultrasensitive detection of molecular biomarkers, with analytical performance beyond the concentration and thermodynamic limits. Instead of screening for

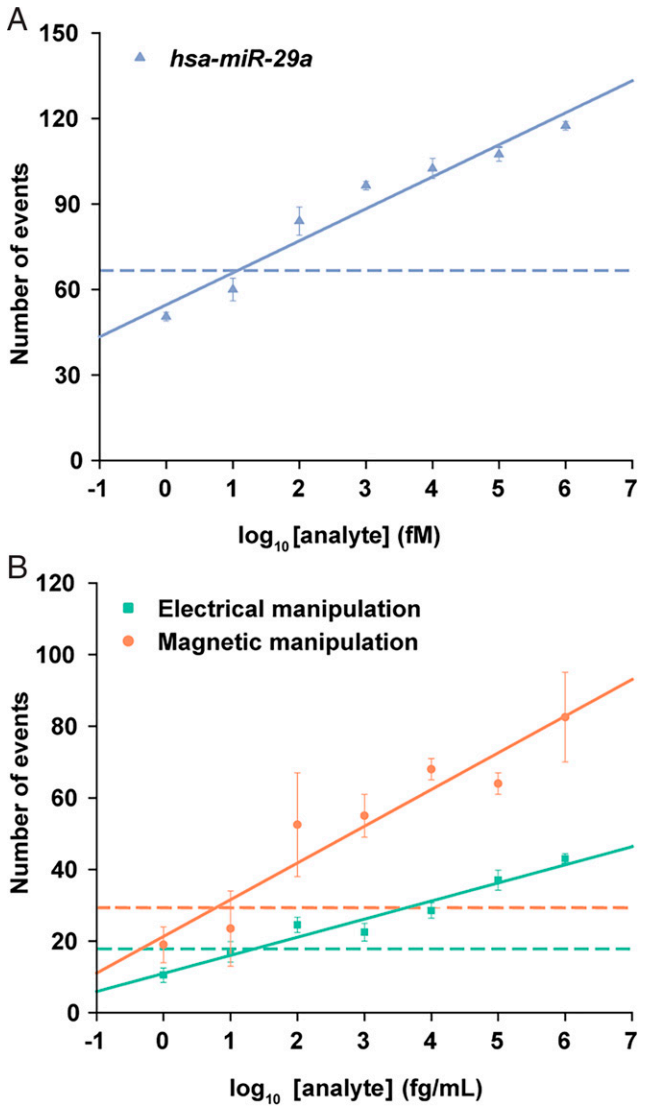

Fig. 5. Detection of miRNAs and proteins spiked in human serum. (*A*) The calibration curve for spiked *hsa-miR-29a* detection in human serum via electrical manipulation with the same protocol as in Fig. 3*A*. (*B*) The calibration curves for spiked $A\beta_{1-42}$ protein detection in pretreated human serum (see *Materials and Methods*) via electrical and magnetic manipulations. The dashed lines indicate the baseline levels in analyte-free human serum.

unique, low-affinity probes in the kinetic fingerprinting approaches, the electrical and magnetic manipulation of nanoparticles allows for fine-tuning of the molecular binding kinetics of high-affinity probes. Compared with the commercialized digital ELISA technique, the SSM[3] is superior in terms of shorter assay time, lower cost, and simpler workflow, benefiting from the usage of heterogeneous, single-molecule information. We anticipate that further improvements on the multiplexing capability, imaging throughput, and finer manipulation could largely advance the wide applications in fundamental biological research and clinical testing.

Materials and Methods

Materials. All oligonucleotides used in this work were synthesized by Sangon Biotech Co., Ltd. Detailed sequences are listed in the *SI Appendix*. Phosphate-buffered saline (PBS) buffer, DEPC-treated water (diethyl pyrocarbonate), and Tris-EDTA buffer were purchased from Sangon Biotech Co., Ltd. The streptavidin-functionalized MNP, Tris-(2-carboxyethyl)-phosphine hydrochloride (TCEP), and sodium dodecyl sulfate (SDS) were purchased from Aladdin. Proteinase K and Tris · HCl buffer were purchased from Beyotime Biotechnology. $A\beta_{1-42}$ peptide and monoclonal antibodies (mAbs) of $A\beta_{1-42}$ (clone 12F4) specific to the C-termini and a mAb capable of binding to the N terminus of $A\beta_{1-42}$ peptide (clone 6E10) were obtained from BioLegend, Inc. The streptavidin-functionalized AuNPs were purchased from Nanopartz. Thiol-Poly(ethylene glycol) (PEG)-hydroxyl (molecular weight: 500 Da) Thiol-PEG-biotin (molecular weight: 3,400 Da), and streptavidin were purchased from Sigma-Aldrich. All solutions were prepared with deionized water (18.2 $M\Omega \cdot cm^{-1}$) from a Millipore system. All experiments were repeated in triplicates unless mentioned otherwise.

Surface Plasmon Resonance Microscopy. The SSM[3] experiments were performed using the previously described SPRM system (26, 27). Briefly, the SPRM was built on an inverted total internal reflection microscope (IX83, Olympus) equipped with a 60× oil-immersion objective. Collimated light from a superluminescent diode (SLD635B, Thorlabs) illuminated the 50 nm Au on BK-7 glass sensor chip at the resonant angle. Images were acquired by a scientific complementary-metal-oxide-semiconductor (sCMOS) camera (Photometrics Prime 95B) with a full field of view of 102.4 × 102.4 μm^2 at a frame rate of 16.7 fps. The image sequences were processed during acquisition by a home-developed software package (40).

Sandwich-Probing Structure. For miRNA detection, the SSM (3) exploited the direct binding of a long-detection, probe-labeled AuNPs to an unlabeled oligoanalyte captured on a Au film. The surface of Au-coated glass slide was passivated with 20 μL Thiol-PEG-hydroxyl spacer at a concentration of 1 μM in 1× PBS for 30 s. Then, the slide was rinsed three times with 1× PBS and incubated with 20 μL 50-nM thiolated single strand DNA (ssDNA) capture probes in 1× PBS solution for 2 h. The capture probe was pretreated with 1 mM TCEP to reduce the thiol groups and activate the thiolated DNA. The surface was finally passivated by adding 20 μL spacer solution, incubated for 20 min, and rinsed with 1× PBS three times to remove the unbound molecules. As for protein sensing, the ssDNA capture probe was replaced by the biotinylated antibody. In brief, the planar sensor surface was first modified with Thiol-PEG-biotin at the concentration of 1 μM in 1× PBS for 15 min, followed by incubation in 1 mg/mL streptavidin in Tris · HCl buffer for 1 h. An mAb probe (clone 6E10) at a concentration of 5 μg/mL was added and incubated for 2 h.

The 50 nm streptavidin-coated AuNP (C11-50-TS-PBS-50-1) at a concentration of 10^{10} NPs/mL was incubated with 100 μL biotinylated DNA detection probe or biotinylated antibody (clone 12F4) at a concentration of 1 μM in 3 mM PBS for 30 min. To note, 40× diluted PBS with an ionic concentration of 3 mM was used to prevent the AuNPs from aggregation. For miRNA detection, the detection probe has the adjustable, complementary length to oligoanalyte. AuNPs were rinsed by 3 mM PBS three times to remove the redundant DNA and diluted to 10^{10} NPs/mL. For magnetic manipulation, the 300 nm streptavidin-coated MNP (S8040-A300nm-1EA) at a concentration of 10^9 NPs/mL was incubated with biotinylated antibody (clone 12F4) for 2 h, at a final concentration of 2.5 μg/mL in Tris · HCl buffer. The mAb-coated MNPs were centrifuged and resuspended for three times to remove the redundant reagent.

Micromanipulation System. The electrical micromanipulation system was built with an electrochemical workstation (CHI660e, CH Instruments Inc.). The counter electrode (CHI115 platinum wire) and reference electrode (CHI111 Ag/AgCl) were placed in a silicon solution cell (flexi-PERM, SARSTEDT), and the Au film served as the working electrode. The voltage is applied between working electrode and reference electrode. For verification of the effect in tuning binding kinetics, the voltage was scanned from −0.4 to +0.4 V. For magnetic micromanipulation, a magnet was placed above the reaction well at a distance controlled by a motored stage to adjust the amplitude of magnetic field.

The 15-min Assay. For a 15-min miRNA assay, all RNA samples were protected from RNase by DEPC-treated water and 1% (weight/volume percentage [wt/vol]) SDS. DEPC treatment was essential for detection of miRNA. A total of 1 μL synthetic analyte miRNA was added into the 19-μL buffer containing detection–probe-conjugated AuNPs at 10^{10}/mL and diluted to gradient concentrations from 10^{-1} to 10^7 fM. The mixture was injected into the reaction well immediately, and the SPRM continuously recorded the nanoparticle images for 15 min. During image recording, a +0.4 V voltage was applied for the first 5 min, followed by a −0.2 V voltage for 10 min. For single–base pair mismatch experiments, *miR-29a* and *miR-29c* were mixed at the concentration ratio of 1:100 before being mixed with the AuNPs. The detection probe was designed to be 12-nt complementary to *miR-29a*. Immunoassay via electrical manipulation follows a similar workflow. For immunoassay with magnetic manipulation, 1-μL $A\beta_{1-42}$ peptide sample was added into the 19-μL buffer containing 10^9 NPs/mL MNP and finally diluted to a gradient concentration of

1 to 10^6 fg/mL. A stack of neodymium magnets was placed at ~2.5 cm above the reaction well at 5 min after the sample was injected.

Spiked Tests in Human Serum. This study was approved by the ethic committee of Shanghai Jiao Tong University. Written informed consent was obtained from the volunteers. The human serum was collected from healthy volunteer and then centrifuged at 1500 rpm for 10 min. The supernatant was recovered, aliquoted, and immediately frozen. 57 μL of freshly thawed human serum was mixed with 1% wt/vol SDS and proteinase K (ST533; final concentration 0.25 μg/mL). After incubation for 30 min at room temperature, the EDTA was added to a final concentration of 20 mM to inhibit the activity of proteinase K. 3 μL of *hsa-miR-29a* or $A\beta_{1-42}$ was added into pretreated-serum to the final concentrations ranging from 1 fM to 1 nM.

The Monte Carlo Simulation of Single-Molecule–Binding Kinetics. The simulation was done using a collection of 200,000 molecules at the temperature of 298 Kelvin. The temporal resolution was 0.02 s, and the viscosity of the solution was set to be 825.9×10^{-6} Pa·S. The higher and lower energy barriers of molecular bound were set as 0.302 K_BT and 0.048 K_BT, respectively.

Data Availability. Data of dynamic particle tracking analysis have been deposited in Mendeley Data (DOI: https://doi.org/10.17632/tfmyf98g7r.1) (41). All other study data are included in the article and/or *SI Appendix*.

ACKNOWLEDGMENTS. This work was funded by the National Natural Science Foundation of China (Grants 22027807 and 61901257) for financial support. We thank Dr. Hongchen Gu and Dr. Hong Xu at Shanghai Jiao Tong University for helpful discussions.

1. B. P. English *et al.*, Ever-fluctuating single enzyme molecules: Michaelis-Menten equation revisited. *Nat. Chem. Biol.* **2**, 87–94 (2006). Correction in: *Nat. Chem. Biol.* **2**, 168 (2006).
2. K. Velonia *et al.*, Single-enzyme kinetics of CALB-catalyzed hydrolysis. *Angew. Chem. Int. Ed. Engl.* **44**, 560–564 (2005).
3. W. E. Moerner, M. Orrit, Illuminating single molecules in condensed matter. *Science* **283**, 1670–1676 (1999).
4. E. Betzig, R. J. Chichester, Single molecules observed by near-field scanning optical microscopy. *Science* **262**, 1422–1425 (1993).
5. B. M. Venkatesan, R. Bashir, Nanopore sensors for nucleic acid analysis. *Nat. Nanotechnol.* **6**, 615–624 (2011).
6. D. Deamer, M. Akeson, D. Branton, Three decades of nanopore sequencing. *Nat. Biotechnol.* **34**, 518–524 (2016).
7. K. M. Mayer, J. H. Hafner, Localized surface plasmon resonance sensors. *Chem. Rev.* **111**, 3828–3857 (2011).
8. P. Zijlstra, P. M. R. Paulo, M. Orrit, Optical detection of single non-absorbing molecules using the surface plasmon resonance of a gold nanorod. *Nat. Nanotechnol.* **7**, 379–382 (2012).
9. W. Fang *et al.*, Quantizing single-molecule surface-enhanced Raman scattering with DNA origami metamolecules. *Sci. Adv.* **5**, eaau4506 (2019).
10. S. Nie, S. R. Emory, Probing single molecules and single nanoparticles by surface-enhanced Raman scattering. *Science* **275**, 1102–1106 (1997).
11. P. Holzmeister, G. P. Acuna, D. Grohmann, P. Tinnefeld, Breaking the concentration limit of optical single-molecule detection. *Chem. Soc. Rev.* **43**, 1014–1028 (2014).
12. T. M. Squires, R. J. Messinger, S. R. Manalis, Making it stick: Convection, reaction and diffusion in surface-based biosensors. *Nat. Biotechnol.* **26**, 417–426 (2008).
13. D. Sevenler, J. Trueb, M. S. Ünlü, Beating the reaction limits of biosensor sensitivity with dynamic tracking of single binding events. *Proc. Natl. Acad. Sci. U.S.A.* **116**, 4129–4134 (2019).
14. S. O. Kelley, What are clinically relevant levels of cellular and biomolecular analytes? *ACS Sens.* **2**, 193–197 (2017).
15. J. J. Gooding, K. Gaus, Single-molecule sensors: Challenges and opportunities for quantitative analysis. *Angew. Chem. Int. Ed. Engl.* **55**, 11354–11366 (2016).
16. Y. Wu, R. D. Tilley, J. J. Gooding, Challenges and solutions in developing ultrasensitive biosensors. *J. Am. Chem. Soc.* **141**, 1162–1170 (2019).
17. Y. Wu, D. Bennett, R. D. Tilley, J. J. Gooding, How nanoparticles transform single molecule measurements into quantitative sensors. *Adv. Mater.* **32**, e1904339 (2020).
18. D. M. Rissin *et al.*, Single-molecule enzyme-linked immunosorbent assay detects serum proteins at subfemtomolar concentrations. *Nat. Biotechnol.* **28**, 595–599 (2010).
19. H. Wang, Z. Tang, Y. Wang, G. Ma, N. Tao, Probing single molecule binding and free energy profile with plasmonic imaging of nanoparticles. *J. Am. Chem. Soc.* **141**, 16071–16078 (2019).
20. S. L. Hayward *et al.*, Ultraspecific and amplification-free quantification of mutant DNA by single-molecule kinetic fingerprinting. *J. Am. Chem. Soc.* **140**, 11755–11762 (2018).
21. A. Johnson-Buck *et al.*, Kinetic fingerprinting to identify and count single nucleic acids. *Nat. Biotechnol.* **33**, 730–732 (2015).
22. T. Chatterjee *et al.*, Direct kinetic fingerprinting and digital counting of single protein molecules. *Proc. Natl. Acad. Sci. U.S.A.* **117**, 22815–22822 (2020).
23. D. Y. Zhang, S. X. Chen, P. Yin, Optimizing the specificity of nucleic acid hybridization. *Nat. Chem.* **4**, 208–214 (2012).
24. W. Jing *et al.*, Time-resolved digital immunoassay for rapid and sensitive quantitation of procalcitonin with plasmonic imaging. *ACS Nano* **13**, 8609–8617 (2019).
25. Y. Wang, W. Jing, N. Tao, H. Wang, Probing single-molecule binding event by the dynamic counting and mapping of individual nanoparticles. *ACS Sens.* **6**, 523–529 (2021).
26. Y. Yang, C. Zhai, Q. Zeng, A. L. Khan, H. Yu, Quantitative amplitude and phase imaging with interferometric plasmonic microscopy. *ACS Nano* **13**, 13595–13601 (2019).
27. Y. Yang *et al.*, Interferometric plasmonic imaging and detection of single exosomes. *Proc. Natl. Acad. Sci. U.S.A.* **115**, 10275–10280 (2018).
28. J. Foote, H. N. Eisen, Kinetic and affinity limits on antibodies produced during immune responses. *Proc. Natl. Acad. Sci. U.S.A.* **92**, 1254–1256 (1995).
29. M. Rief, F. Oesterhelt, B. Heymann, H. E. Gaub, Single molecule force spectroscopy on polysaccharides by atomic force microscopy. *Science* **275**, 1295–1297 (1997).
30. K. C. Neuman, A. Nagy, Single-molecule force spectroscopy: Optical tweezers, magnetic tweezers and atomic force microscopy. *Nat. Methods* **5**, 491–505 (2008).
31. O. K. Dudko, A. E. Filippov, J. Klafter, M. Urbakh, Beyond the conventional description of dynamic force spectroscopy of adhesion bonds. *Proc. Natl. Acad. Sci. U.S.A.* **100**, 11378–11381 (2003).
32. P. Hänggi, P. Talkner, M. Borkovec, Reaction-rate theory: Fifty years after Kramers. *Rev. Mod. Phys.* **62**, 251–341 (1990).
33. X. Shan *et al.*, Imaging the electrocatalytic activity of single nanoparticles. *Nat. Nanotechnol.* **7**, 668–672 (2012).
34. X. Shan, U. Patel, S. Wang, R. Iglesias, N. Tao, Imaging local electrochemical current via surface plasmon resonance. *Science* **327**, 1363–1366 (2010).
35. D. M. Rissin, D. R. Walt, Digital readout of target binding with attomole detection limits via enzyme amplification in femtoliter arrays. *J. Am. Chem. Soc.* **128**, 6286–6287 (2006).
36. W. Jing *et al.*, Gradient-based rapid digital immunoassay for high-sensitivity cardiac troponin T (hs-cTnT) detection in 1 μL plasma. *ACS Sens.* **6**, 399–407 (2021).
37. C. Danilowicz, D. Greenfield, M. Prentiss, Dissociation of ligand-receptor complexes using magnetic tweezers. *Anal. Chem.* **77**, 3023–3028 (2005).
38. A. Nakamura *et al.*, High performance plasma amyloid-β biomarkers for Alzheimer's disease. *Nature* **554**, 249–254 (2018).
39. S. Janelidze *et al.*, Plasma β-amyloid in Alzheimer's disease and vascular disease. *Sci. Rep.* **6**, 26801 (2016).
40. X. Wang *et al.*, Automated nanoparticle analysis in surface plasmon resonance microscopy. *Anal. Chem.* **93**, 7399–7404 (2021).
41. H. Yu, Q. Zeng, Raw data for PNAS Paper. Mendeley Data. 10.17632/tfmyf98g7r.1. Deposited 7 February 2022.